9B.5

APR-2 TROPICAL CYCLONE OBSERVATIONS

S. L. Durden and S. Tanelli
Jet Propulsion Laboratory, California Institute of Technology

1. INTRODUCTION

The Second Generation Airborne Precipitation Radar (APR-2) participated in the Genesis and Rapid Intensification Processes (GRIP) experiment in August and September of 2010, collecting a large volume of data in several tropical systems, including Hurricanes Earl and Karl. Additional measurements of tropical cyclones have been made by APR-2 in experiments prior to GRIP (namely, CAMEX-4 and NAMMA); Table 1 lists all the APR-2 tropical cyclone observations.

The APR-2 observations consist of the vertical structure of rain reflectivity at 13.4 (Ku-band) and 35.6 GHz (Ka-band), and at both co-polarization and cross-polarization, as well as vertical Doppler measurements and crosswind measurements. APR-2 normally flies on the NASA DC-8 aircraft, as in GRIP, collecting data with a downward-looking, cross-track scanning geometry. The scan limits are 25 degrees on either side of the aircraft, resulting in a roughly 10-km swath at the surface, depending on the aircraft altitude. Details of the APR-2 observation geometry and performance can be found in Sadowy et al. (2003).

The multiparameter nature of the APR-2 system makes its observations valuable for detailed studies of the processes, microphysics and dynamics of tropical cyclones, as well as weaker systems that are associated with tropical cyclone formation. In this paper, we give a brief overview of how the APR-2 data are processed. We also discuss use of the APR-2 cross-track winds to estimate various quantities of interest in in studies of storm intensification. Finally, we show examples of the standard products and derived information.

2. APR-2 DATA PROCESSING

The standard APR-2 data processing first requires that the radar data be synchronized with the aircraft navigation data. For GRIP both the standard aircraft data and higher-quality GPS data from the MMS instrument suite were collected. The navigation data are used to estimate the aircraft orientation, providing a Doppler correction for the data. This correction is also estimated from the radar surface return's Doppler (Durden et al. 1999). Generally, the two approaches compare quite well, and the surface Doppler is normally used, but the navigation-estimated correction is also provided in the standard data product.

Corresponding author address: 4800 Oak Grove Dr., Pasadena, CA 91109; email: sdurden@jpl.nasa.gov.

Table 1. APR-2 tropical cyclone observations

Date	Tropical Cyclone
8/20/01	TS Chantal
9/15	TS Gabrielle
9/22	TS Humberto
9/23	H Humberto
9/24	H Humberto
8/23/06	TS Debby
9/12	Depression Helene
8/29/10	H Earl
8/30	H Earl
9/1	H Earl
9/2	H Earl
9/14	TS Karl
9/16	H Karl
9/17	H Karl

The radar data are initially calibrated using data recorded through a calibration loop in the radar. Final calibration is based on the ocean backscatter at 10 degrees for Ku-band. At this incidence angle, the surface return is least sensitive to wind speed. The Ka-band calibration is then adjusted to agree with the Ku-band measurements in very light precipitation, based on Mie scattering calculations. The APR-2 calibration is described in more detail in Tanelli et al. (2006).

APR-2 records both the co-polarized and cross-polarized return at both frequencies. From these measurements we estimate the linear depolarization ratio (LDR). By using the Doppler measurements over a scan and assuming horizontal uniformity at each altitude, we can solve for the vertical and horizontal velocity components at each altitude. For reasonably well-organized tropical cyclones, we were typically flying radial tracks, so the cross-track wind serves as an estimate of the cyclone's azimuthal wind. In reality, the radial may not be exact, and the aircraft is likely yawed, so the cross-track direction deviates from the azimuthal direction relative to storm center. Here, we ignore such errors.

3. ADDITIONAL QUANTITIES OF INTEREST

In this section we discuss several quantities that can be derived from the standard products.

We can infer the location of melting ice from the LDR parameter noted above. We can also form the difference of the Ku-band and Ka-band reflectivities. In ice, one expects low attenuation and small difference between the two reflectivities if the ice particles are small. However, as the particles increase in size, they leave the Rayleigh scattering regime at Ka-band. Their reflectivity decreases relative to Ku-band, so ZKu-ZKa (in dB) can reach several dB (Heymsfield et al. 2006). This dual-wavelength ratio (DWR) is useful in identifying areas with larger ice particle sizes. At lower altitudes in rain, the particle size is a minor contributor to DWR. The major contribution comes from the differential attenuation between Ku- and Ka-band. Thus, in rain, large DWR indicates strong attenuation and heavy rainfall.

The inertial frequency in a vortex is the usual Coriolis frequency f modified by the vortex. It is:

$$I^2 = (f + \frac{2v}{r})(f + \frac{v}{r} + \frac{\partial v}{\partial r}) \qquad (1)$$

where v is the azimuthal velocity. As the inertial frequency increases, the vortex stiffens, making it easier for energy from latent heating to go into the transverse circulation, rather than going into oscillations and being radiated away. Specifically, one can examine the Rossby length (Vigh and Schubert 2009), which is the internal gravity wave speed divided by I. The Rossby length (or Rossby radius) is the length at which rotational effects become as important as buoyancy effects. Another quantity related to I is the Ekman layer thickness, defined as the square root of twice the eddy viscosity divided by I (Kepert 2001). For these calculations, we assume a gravity wave speed of 100 m/s and an eddy viscosity of 50 m^2/s.

Also of interest is the warm-core structure of the storm. While radar isn't directly sensitive to density or thermal structure, such structure can be inferred by assuming an axisymmetric vortex in gradient and hydrostatic balance. Smith (2006) derives a method to estimate the pressure, density, and temperature structure under such assumptions, given the azimuthal wind field, as a function of radius and altitude. To do so, he derives a thermal wind equation and then uses the anelastic approximation:

$$\frac{\partial p}{\partial r} = \rho_o(\frac{v^2}{r} + fv) \qquad (2)$$

$$\frac{\partial \rho}{\partial r} = -\frac{1}{g}\frac{\partial}{\partial z}\left[\rho_o(\frac{v^2}{r} + fv)\right]$$

In these equations, p is pressure, ρ is density, ρ_0 is environmental density, g is gravitational acceleration, f is the Coriolis parameter, and v is the azimuthal velocity. The surface pressure is 1013 hPa and the surface density is 1.2 kg/m^3. A constant lapse rate of 6.5 K/km is used for the environmental temperature profile. We use a finite difference approximation and then integrate at each altitude to get pressure and density versus radius. Then temperature anomaly is derived using the ideal gas law, then subtracting the environmental temperature.

4. OBSERVATIONS

This section examines the APR-2 standard products and derived quantities for Hurricanes Earl and Karl of 2010.

4.1 *Hurricane Earl*

Earl became a tropical storm on 8/25 when it was located to the west of the Cape Verde Islands. It continued across the Atlantic at tropical storm strength, followed by a period of rapid intensification, reaching Category 1 on the Saffir-Simpson scale on the 29th and Category 4 on the 30th. Its Intensity fluctuated over the next two days, dropping to Category 3 and then reaching its maximum Category 4 intensity on 9/1. As it moved to higher latitudes, it was impacted by southerly shear and weakened. APR-2 data were acquired on 8/29, 8/30, 9/1, and 9/2. Here we concentrate on the rapid Intensification period of 8/29 and 8/30.

Figures 1 and 2 show the Ku-band reflectivity, Ku-band LDR, Ka-band reflectivity, and the DWR for both days. Although the eye was not particularly distinct visually on the 29th (at least from the DC-8 altitude), it does appear In the APR-2 data at 20:29:52 UTC. The flight track was east to west, and the stronger convection appears to the east of the eye (left side of the image). On this side, the strongest convection is adjacent to the eye. Peak reflectivity is at least 45 dBZ, and strong attenuation can be seen at Ka-band in several locations; white areas just above the surface indicate poor SNR due to attenuation. Based on the Ka-band data and the DWR, the rainfall in the eyewall was somewhat greater on the 30th, whereas the outer convection had reduced in intensity. Inspection of 85 GHz passive microwave imagery shows that Earl went through several phases of asymmetry. It appears more symmetric early on the 30th and then later following the APR-2 data acquisition. We can hypothesize that the asymmetry in the APR-2 measurements is a convective burst related to the intensification (Harnos and Nesbitt 2011, and references therein).

Figures 3 and 4 show the corresponding wind data. The yellow and red areas at upper levels in the vertical motion image just to the left of the eye indicate fairly strong updrafts (>10 m/s). The

occurrence of the updraft maximum at high altitude is consistent with the ideas of Zipser (2003). The XWIND image (azimuthal velocity) shows several maxima; it can be argued that the strongest convection is inside the radius of maximum wind. According to Vigh and Schubert (2009), this allows the heating from the convection to better contribute to the storm's secondary circulation and intensification. Calculations of the Rossby length indicate that it decreases from an environmental value of more than 1000 km to a roughly 100 km near the center. This indicates that the heating at the center is located in a vortex that is stiffening. We also computed this same quantity from flight level wind measurements from an Air Force reconnaissance flight and found a similar result. On the 30th the Rossby length Is even smaller near the center. As discussed by Zhang et al. (2011) the boundary layer thickness decreases toward the center, as also seen in Figure 5 and 6.

Figures 6 and 7 shows the CFAD for ZKu (i.e., reflectivity histogram at each altitude) in the inner core region, along with CFADs for the vertical and azimuthal velocities. The CFAD for azimuthal velocity is bimodal, since velocities on opposite sides of center have opposite signs. The vertical velocities on the two days are fairly similar, while the peak reflectivity is several dBZ larger on the 30th. The measured azimuthal winds are, of course, significantly larger on the 30th, with peak near 55 m/s.

The last panels in Figures 3 and 4 are the pressure deficit derived from Smith's method using (2a). The maximum pressure deficit in the eyewall on the 29th is around 35 hPa, fairly consistent with a minimal hurricane. The central pressure was near 975 hPa, as measured by aircraft dropsonde. The retrieved pressure deficit on the 30th (Figure 4) is 65 hPa, consistent with dropsonde measurements near and just below 950 hPa.

Using Smith's method and the pressure field, we also retrieved the density and temperature anomaly. These are shown for both days in Figures 9 and 10, with the upper image being density and the lower being temperature anomaly. The basic structure seems qualitatively correct. The temperature anomaly, for example, is somewhat similar to the structure of Hurricane Inez and shown in Hawkins and Imbembo (1976). Dropsonde data from the DC-8 on the 30th indicated a temperature anomaly of around 13 K at 300 hPa.

4.2 *Hurricane Karl*

Karl also formed from a disturbance that originated in the eastern Atlantic. However, its path was south of Earl's, entering the eastern Caribbean Sea as a disturbance and, after defying forecasts, finally becoming a depression and tropical storm on 9/14. Figure 11 shows the Ku-band reflectivity and crosswind images from 9/14. An apparent circulation with center determined by the change in winds from positive to negative is visible in the crosswind image. This image is consistent with a vortex with maximum winds of 15-20 m/s, which is on the borderline between tropical depression and tropical storm. At the time of the APR-2 data acquisition, the area did not have intense convection; the reflectivity shows mostly stratiform rainfall, based on the existence of a bright band in the reflectivity image.

ACKNOWLEDGEMENT

This study was carried out at the Jet Propulsion Laboratory, California Institute of Technology, under a contract with the National Aeronautics and Space Administration.

REFERENCES

Durden, S. L., Z. S. Haddad, and T. P. Bui, 1999: Correction of Doppler radar data for aircraft motion using surface measurements and recursive least-squares estimation. *J. Atmos. Oceanic Technol.*, **16**, 2026-2029.

Hawkins, H. F. and S. M. Imbembo, 1976: The structure of a small, intense hurricane – Inez 1966. *Mon. Wea. Rev*., **104**, 418-442.

Heymsfield, A. J., A. Bansemer, S. L. Durden, R. L. Herman, and T. P. Bui, 2006: Ice microphysics observations in Hurricane Humberto: Comparison with non-hurricane-generated ice cloud layers. *J. Atmos. Sci*., **63**, 288-308.

Harnos, D. S., and S. W. Nesbitt, 2011: Convective structure in rapidly intensifying tropical cyclones as depicted by passive microwave measurements. *Geophys. Res. Lett*, **38**, L07805, doi10.1029/2011GL047010.

Kepert, J., 2001: The dynamics of boundary layer jets within the tropical cyclone core. Part I: Linear theory. *J. Atmos. Sci.*, **58**, 2469-2484.

Sadowy, G. A., A. C. Berkun, W. Chun, E. Im, and S. L. Durden, 2003: Development of an advanced airborne precipitation radar. *Microwave J*., **46**, 84-98.

Schubert, W. H, and B. D. McNoldy, 2010: Application of the concepts of Rossby length and Rossby depth to tropical cyclone dynamics. *J. Adv. Model Earth Syst*., **2**, 7.

Smith, R. K., 2006: Accurate determination of a balanced axisymmetric vortex in a compressible atmosphere. *Tellus*, **58A**, 98-103.

Tanelli, S., S. L. Durden, and E. Im, 2006: Simultaneous Measurements of Ku- and Ka-band Sea Surface Cross-Sections by an Airborne Radar. *IEEE Geosci. Remote Sens. Lett*.,. **3**, 359-363.

Vigh, J. L., and W. H. Schubert, 2009: Rapid development of the tropical cyclone warm core. *J. Atmos. Sci*., **66**, 3335-3350.

Zhang, J. A., R. F. Rogers, D. S. Nolan, and F. D. Marks, 2011: On the characteristic height scales of the hurricane boundary layer. *Mon.Wea. Rev.*, **139**, 2524-2535.

Zipser, E., 2003: Some views on “hot towers” after 50 years of tropical field programs and two years of TRMM data. *Meteorological Monographs*, **29**, 49–58.

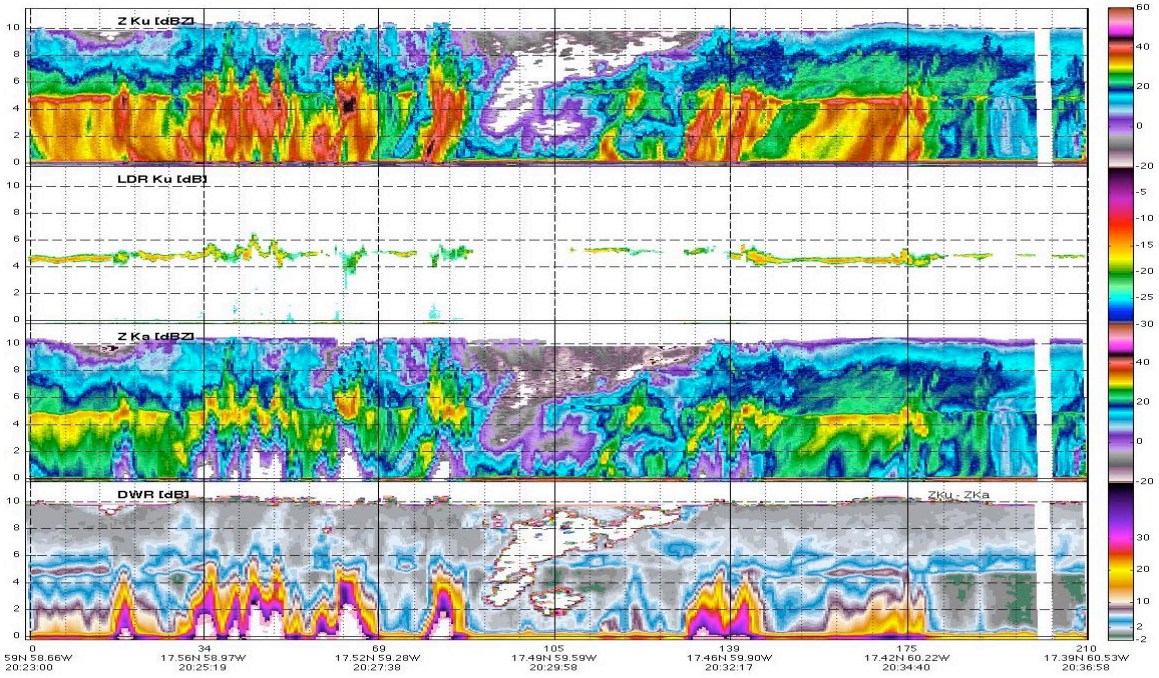

Figure 1. APR-2 measurements of Hurricane Earl on August 29, 2010

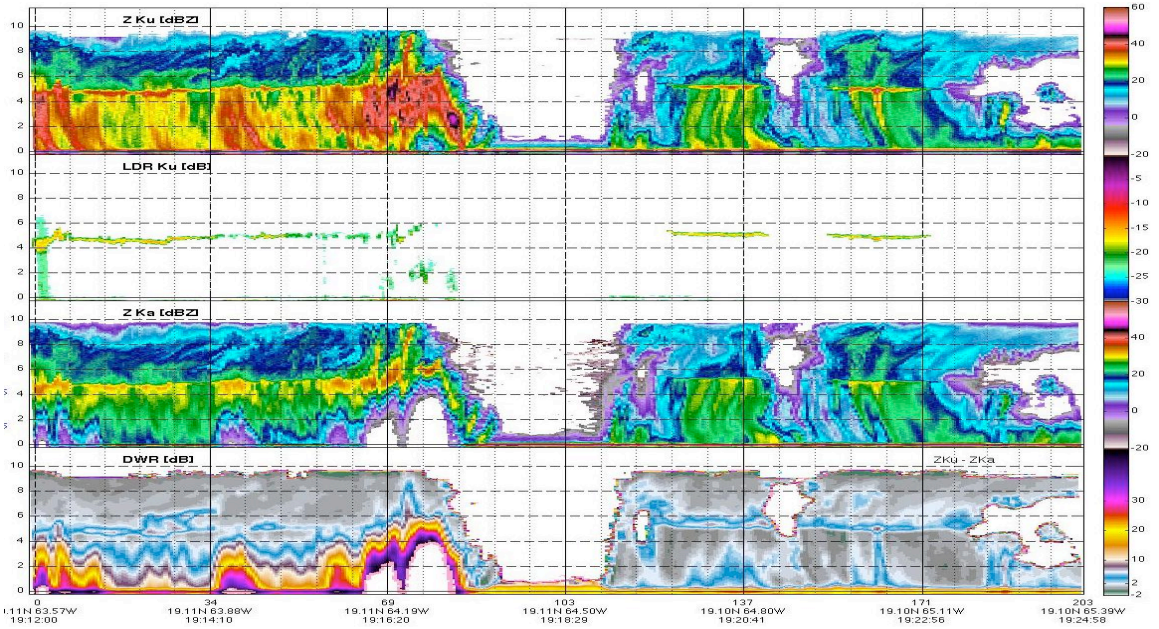

Figure 2. APR-2 measurements of Hurricane Earl on August 30, 2010

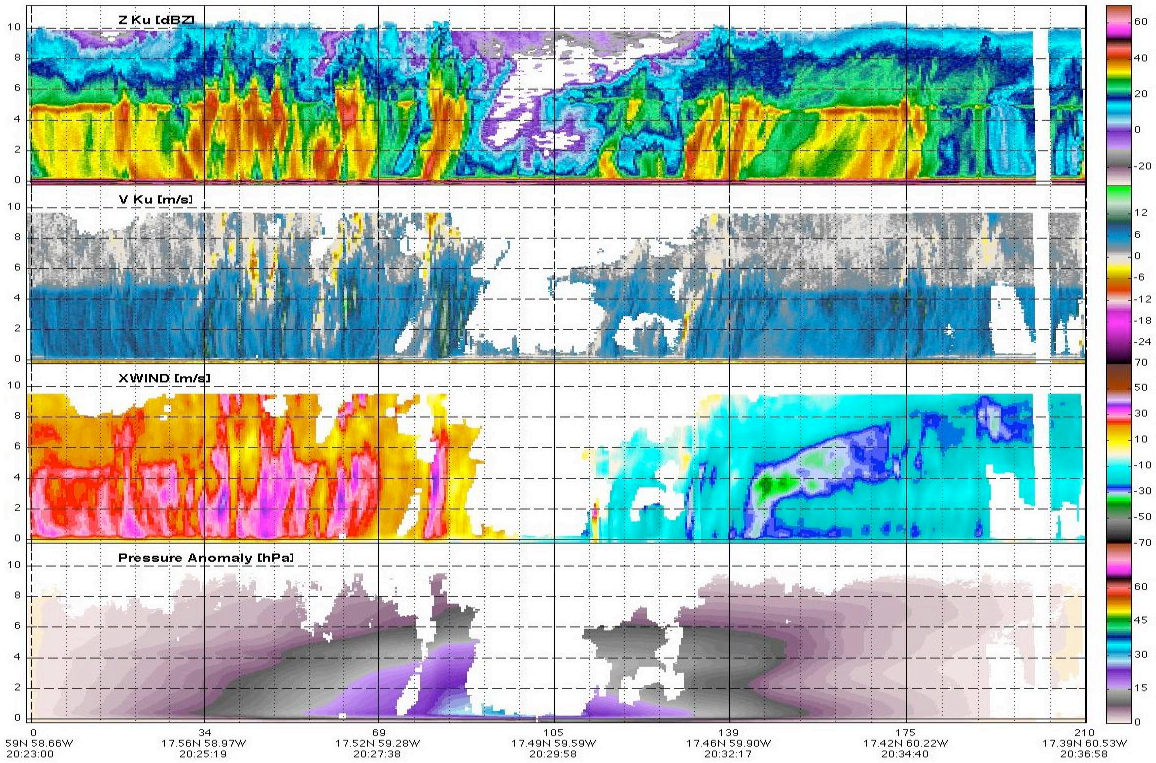

Figure 3. APR-2 measurements of Hurricane Earl on August 29, 2010

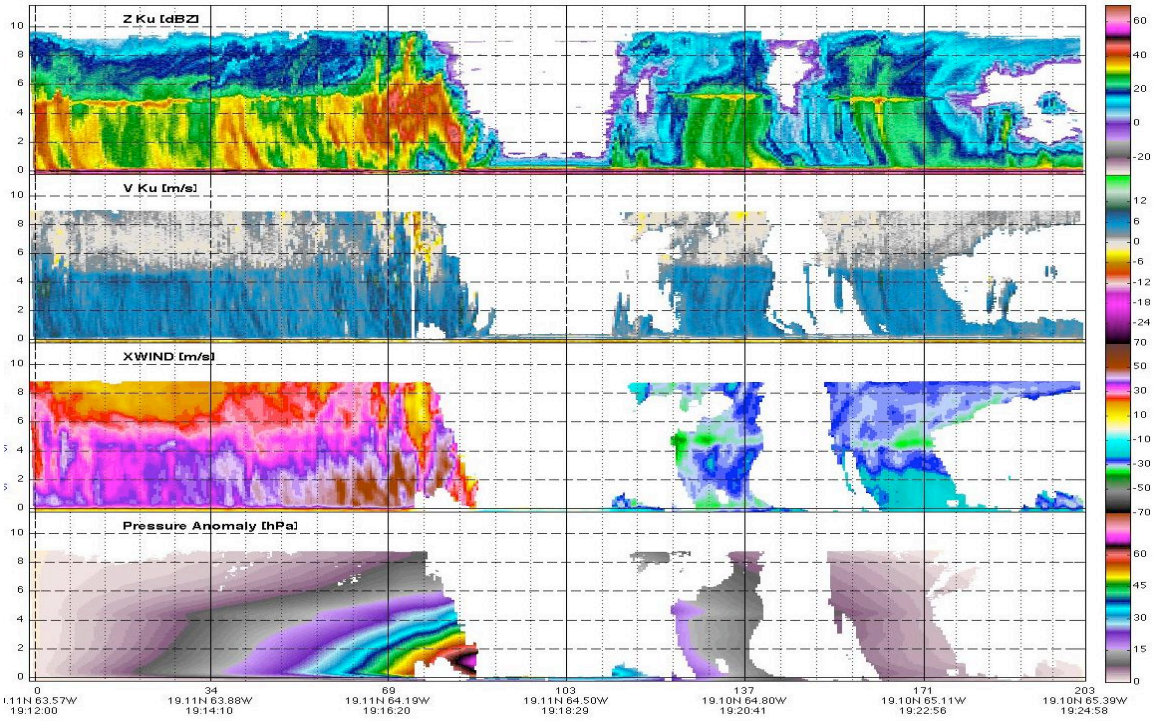

Figure 4. APR-2 measurements of Hurricane Earl on August 30, 2010

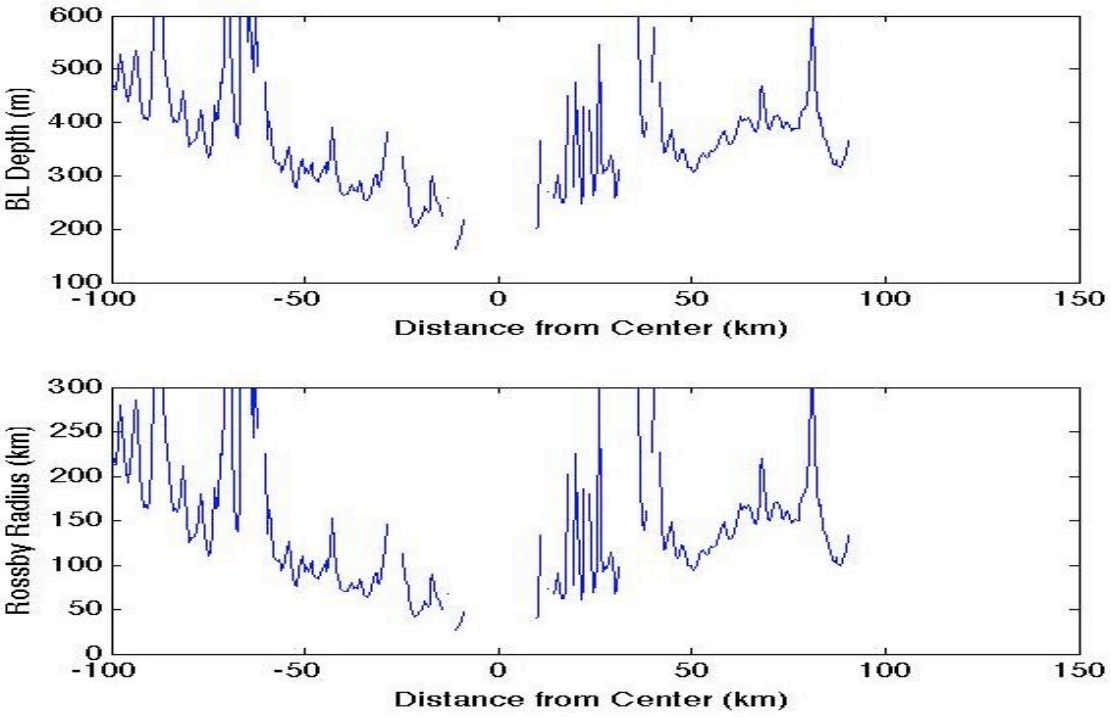

Figure 5. Ekman boundary layer depth and Rossby length in Earl on August 29.

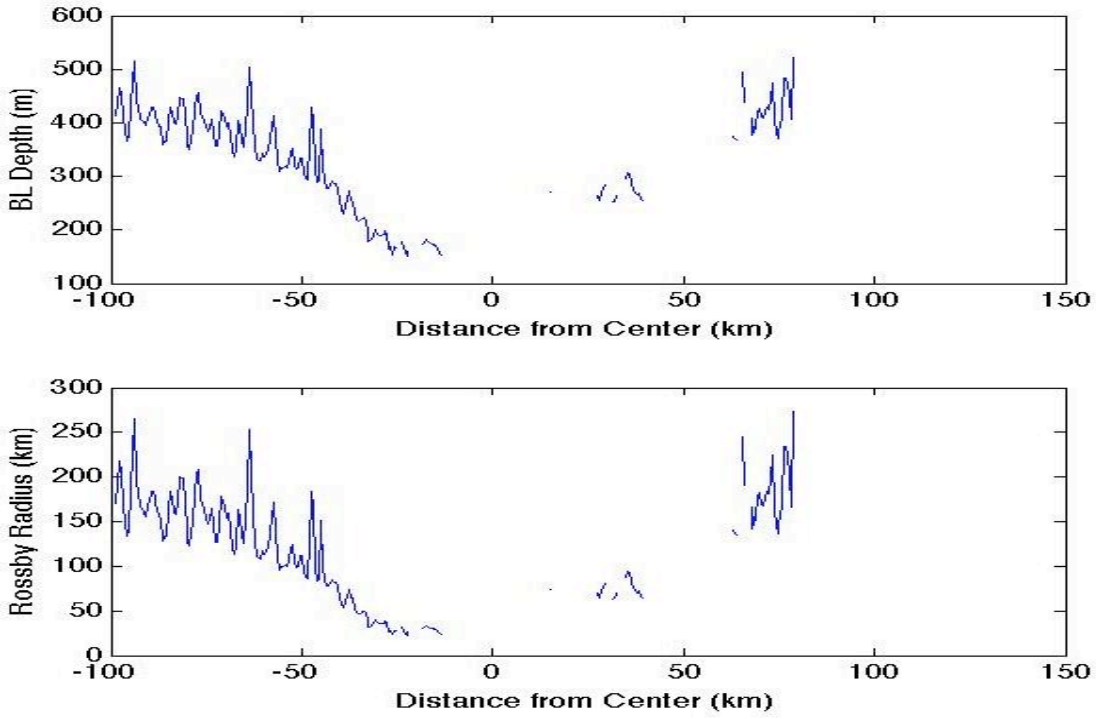

Figure 6. Ekman boundary layer depth and Rossby length in Earl on August 30.

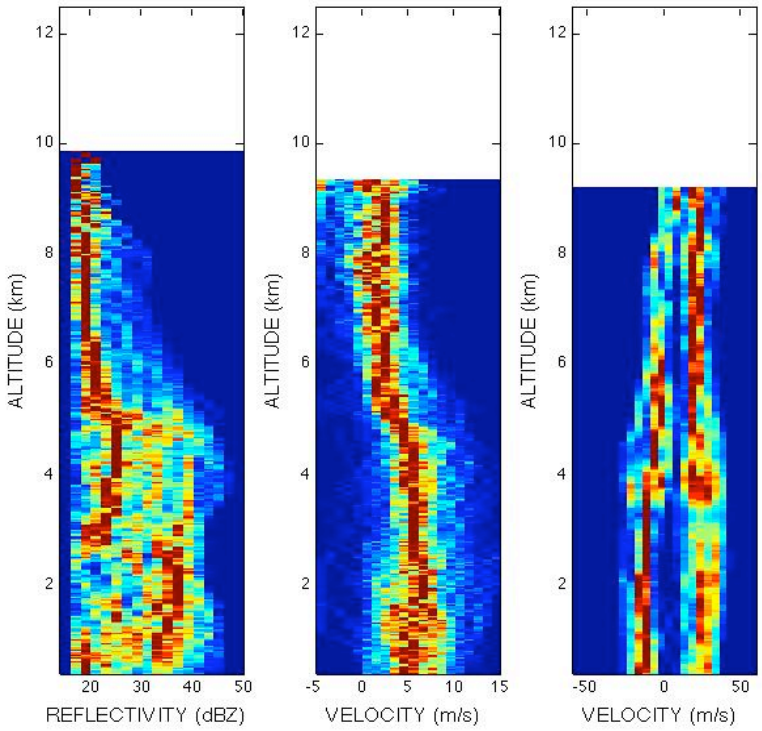

Figure 7. CFADs for reflectivity (left), vertical velocity (middle), and azimuthal velocity (right) for Hurricane Earl on August 29, 2010.

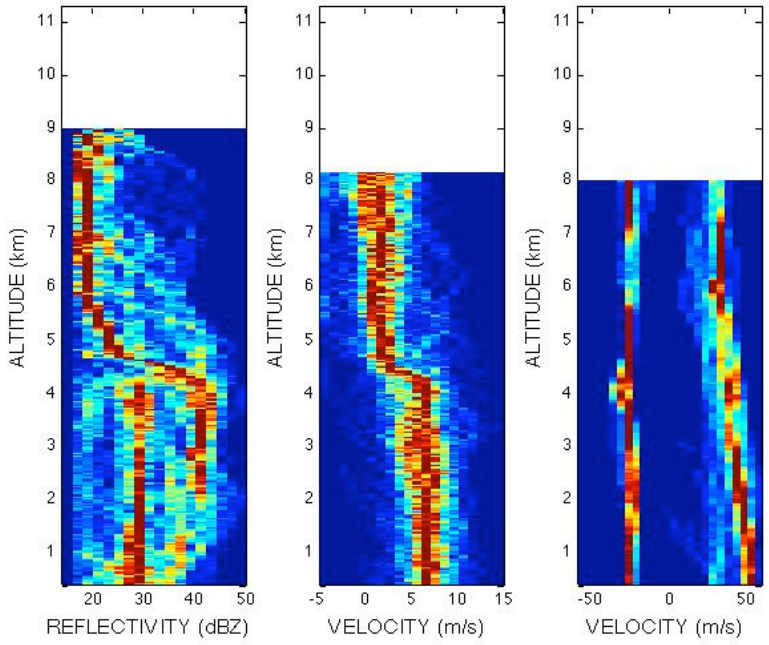

Figure 8. CFADs for reflectivity (left), vertical velocity (middle), and azimuthal velocity (right) for Hurricane Earl on August 30, 2010.

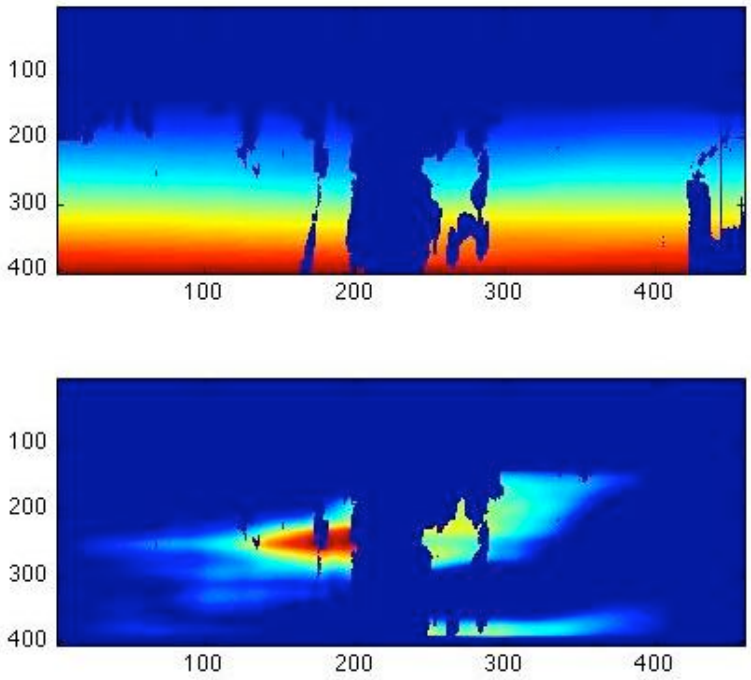

Figure 9. Density (upper) and temperature anomaly (lower) for Earl on Aug 29.
Maximum values are in red.

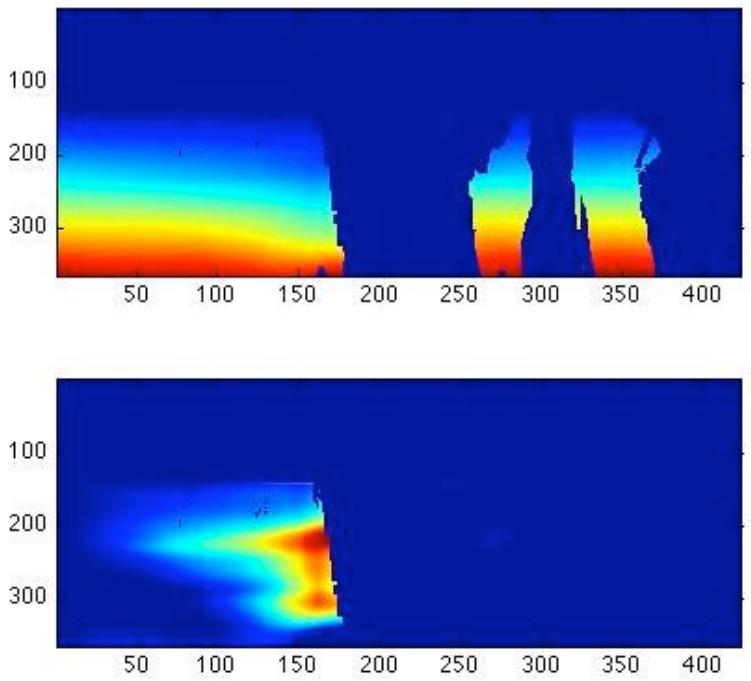

Figure 10. Density (upper) and temperature anomaly (lower) for Earl on Aug 30.
Due to low SNR on the right side, the temperature anomaly is valid only on the left.

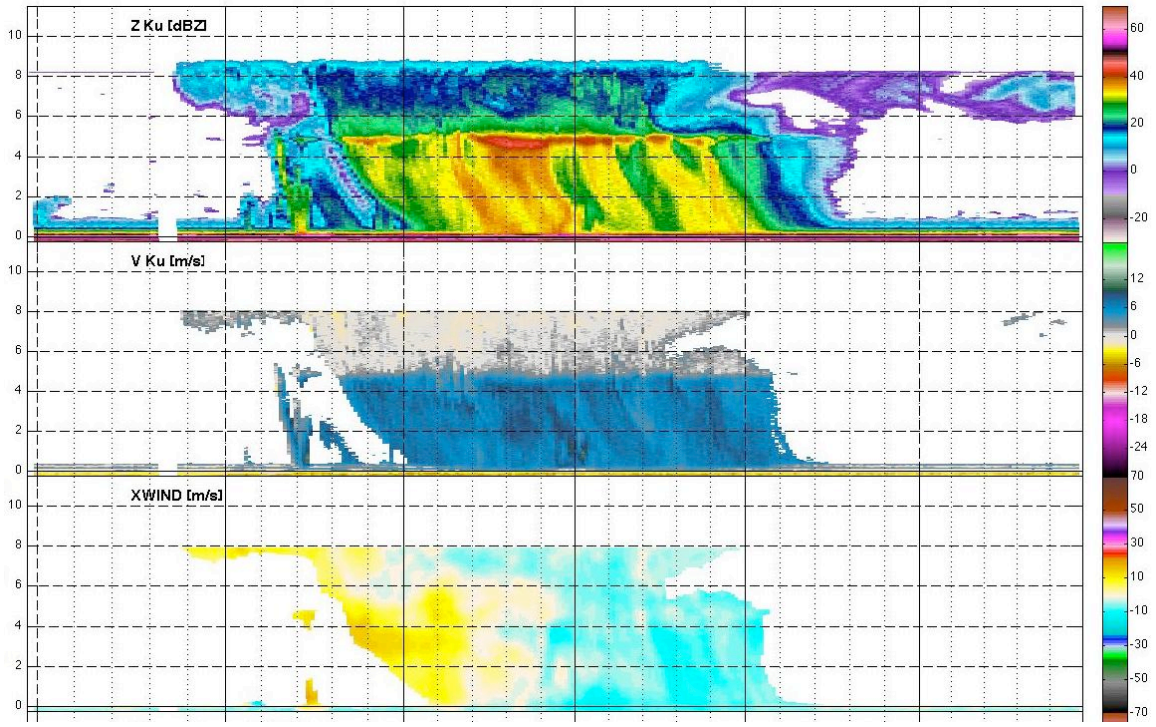

Figure 11. Reflectivity, vertical velocity of hydrometeors, and azimuthal velocity in Karl as it was becoming a tropical storm. A weak circulation can be seen in the bottom image, with center seen as the change in color from yellow to blue. Location is 18 N and 84 W on September 14 at 20:35 UTC.